Supporting information

Speciation and dipole re-orientation dynamics of glass-forming liquid electrolytes: $Li[N(SO_2CF_3)_2]$ mixtures of 1,3-propanesultone or tetrahydrothiophene-1,1-dioxide.

Yasuhiro Umebayashi[1,*], Erika Otani[1], Hikari Watanabe[2], Jihae Han[1]

[1] Graduate School of Science and Technology, Niigata University, 8050 Ikarashi, 2-no-cho, Nishi-ku, Niigata, 950-2181, Japan; E-mail: yumescc@chem.sc.niigata-u.ac.jp
[2] Department of Pure and Applied Chemistry, Faculty of Science and Technology, Tokyo University of Science, 2641 Yamazaki, Noda, Chiba 278-8510, Japan

Experimental

Materials 1,3-propanesultone (PS) or tetrahydrothiophene-1,1-dioxide (SL) were purchased from Tokyo Chemical Industry Co., Ltd.. Anhydrous LiTSFA (TFSA = $(CF_3SO_2)_2N^-$) supplied by Solvey. The mixture of LiTFSA and solvent were stirred overnight to obtain transparent solutions in an Ar glovebox.

Ionic conductivity, viscosity and density Ionic conductivity was measured with a conductivity meter HORIBA DS-51 and F-55 conductivity meter with the platinum black electrodes HORIBA 3552-10D. The cell constant was determined using aqueous KCl solutions (0.005, 0.01, 0.1, 0.25, 0.50, 0.75, 1.0 mol dm^{-3}) at 298 K [1]. Viscosity and density were measured with an Anton Paar Stabinger Viscometer SVM 3000.

Self-diffusion coefficients The self-diffusion coefficients of ^1H, ^7Li and ^{19}F for LiTFSA-PS and LiTFSA-SL systems were measured using a JEOL ECX400 with a narrow-bore 9.39 T superconducting magnet and equipped with a pulsed-field gradient multiprobe. The self-diffusion coefficient (D) was obtained using Stejskal and Tanner equation for homogeneous systems [2] as follows:

$$E = exp\left(-\gamma^2\delta^2 g^2 D\left(\Delta - {}^{\delta}/_{3}\right)\right)$$

, where γ, δ, g, Δ are gyromagnetic ratio of the observed nuclei, duration time of the pulsed-field gradient, amplitude and the diffusion time, respectively.

Differential scanning calorimetry and thermogravimetry Differential scanning calorimetry (DSC) and thermogravimetry were carried out under Ar gas at 5 K min^{-1} by using Rigaku Thermo plus EVO2 DSCvesta and Rigaku Thermo plus EVO2 TG-DTA8122.

Raman spectroscopy Raman spectra for both systems were measured using a JASCO RMP–510 Raman spectrometer equipped with a single monochromator and CCD detector at an optical resolution of about 2.7 cm^{-1}. For excitation, a Coherent Inova 70 Ar+ laser was used at 514.5 nm and was operated at 400 mW.

Dielectric relaxation spectroscopy Dielectric relaxation spectra were achieved with a Keysight N5234B vector network analyzer and Agilent E4991A impedance analyzer combined with N1501A-101 probe. The probe was mounted in the PTFE cells. [4] A cell temperature was maintained at 298 K. The calibration was carried out using open, short and load. The load was a reference solvent, which used distilled water and dimethylacetamide. [5-7] A generalized complex permittivity, $\varepsilon(\nu) = \varepsilon'(\nu) - i\,\varepsilon''(\nu)$, where $\varepsilon'(\nu)$ and $\varepsilon''(\nu)$ are real and imaginary permittivity, respectively, was obtained from 30 MHz to 43.5 GHz.

Theoretical calculations The geometries of the isolated solvent, TFSA anion and possible Li-ion complexes were optimized and their theoretical Raman bands were calculated at the B3LYP/cc-pVDZ level by using Gaussian 16. [3]

Raman/DRS two dimensional correlation analysis

Pearson correlation coefficients were calculated between the apparent Raman band intensity $I_{c\mathrm{Li}}$ and the dielectric loss $\varepsilon''_{c\mathrm{Li}}$ as follows,

$$r(\varepsilon''_{c_{Li}}, I_{c_{Li}}) = \frac{\sum(\varepsilon''_{c_{Li}} - \varepsilon''_{avg})(I_{c_{Li}} - I_{avg})}{\sqrt{\sum(\varepsilon''_{c_{Li}} - \varepsilon''_{avg})^2 \sum(I_{c_{Li}} - I_{avg})^2}}$$

, where I_{avg} and $\varepsilon''_{\mathrm{avg}}$ are the averages for the apparent Raman band intensity and the dielectric loss, respectively. The apparent Raman band intensity is calculated as the normalized Raman band intensity divided by the scattering species concentration to make changes in chemical species easier to recognize at a glance.

Noda-Ozaki 2D hetero-correlation spectroscopy

Noda-Ozaki 2D hetero-correlation spectrum between the apparent Raman band intensity and the dielectric loss spectra can yield two kinds of correlations called synchronous $\Phi(\nu_D,\nu_R)$ and asynchronous $\Psi(\nu_D,\nu_R)$ spectra as follows, [8]

$$\Phi(\nu_D,\nu_R) = \frac{1}{m-1}\sum_{j=1}^{m} \tilde{D}_j(\nu_D)\tilde{R}_j(\nu_R)$$

$$\Psi(\nu_D,\nu_R) = \frac{1}{m-1}\sum_{j=1}^{m} \tilde{D}_j(\nu_D)\tilde{o}_j(\nu_R)$$

, where m is the number of the spectra, ν_{D} and ν_{R} are the frequency of DRS and wavenumber of the Raman spectra, respectively, $\tilde{D}_j(\nu_D)$ and $\tilde{R}_j(\nu_R)$ are dynamic spectra at jth DRS and Raman spectra in molar ratio of Li salt $x_{\mathrm{Li},\,j}$, respectively, given by the following equation.

$$\tilde{D}_j(\nu_D) = D_j(\nu_D, x_{Li}) - \bar{D}_{\nu_D}$$

$$\tilde{R}_j(\nu_R) = R_j(\nu_R, x_{Li}) - \bar{R}_{\nu_R}$$

, where $D_j(\nu_D, x_{Li})$ and $R_j(\nu_R, x_{Li})$ are the dielectric loss spectra and the apparent Raman band, respectively, $\bar{D}_{\nu_D}$ and $\bar{R}_{\nu_R}$ are the average spectra of the dielectric loss spectra and the apparent Raman band, respectively.

For asynchronous $\Psi(\nu_D,\nu_R)$ spectra, the orthogonal spectra $\tilde{o}_j(\nu_R)$ can be obtained from the dynamic spectra $\tilde{R}_j(\nu_R)$ by using linear transformation operation given by the following equation.

$$\tilde{o}_j(\nu_R) = \sum_{k=1}^{m} n_{jk}\tilde{R}_k(\nu_R)$$

, where n_{ij} is the element of the *Hilbert-Noda transformation matrix* [9]

$$n_{jk} = \begin{cases} 0 & if\ j = k \\ \dfrac{1}{\pi(k-j)} & otherwise \end{cases}$$

Noda-Ozaki 2D hetero-correlation spectra were calculated by using the 2DShige version 1.3 software. [10]

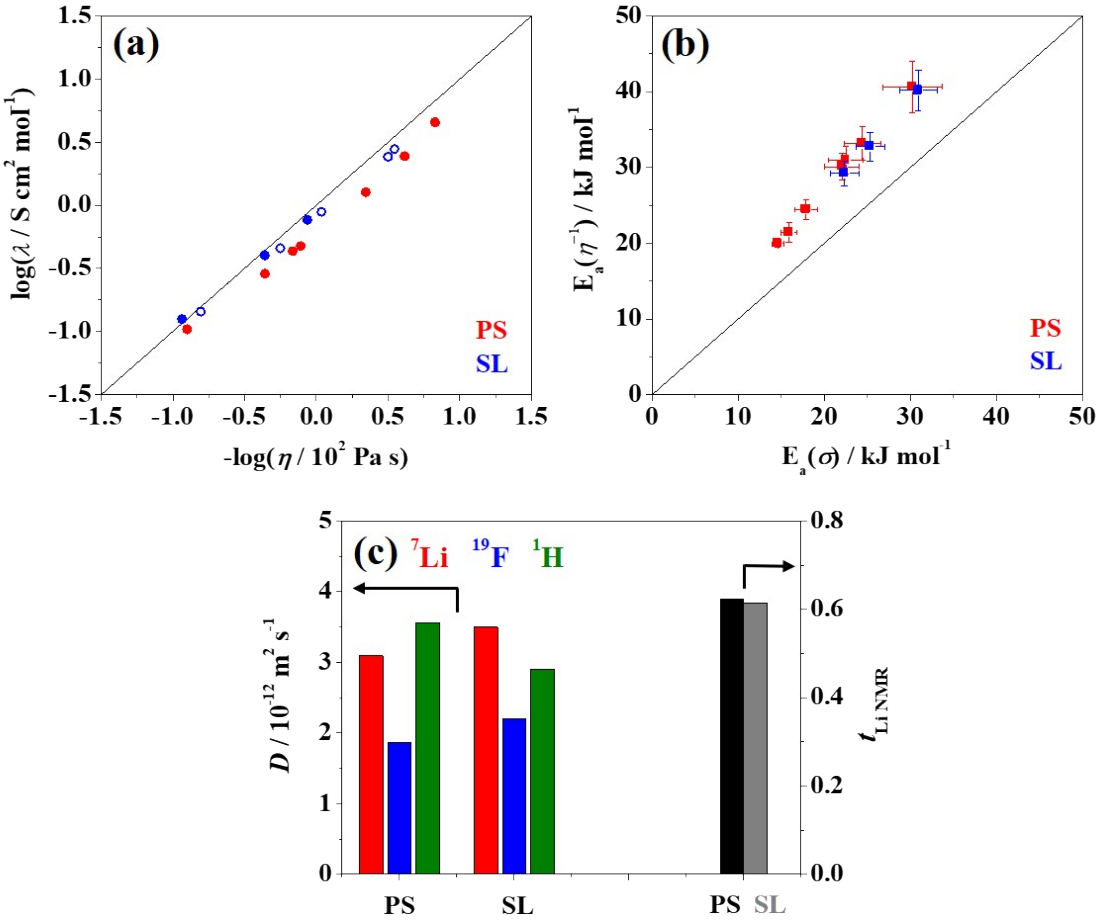

Fig. S1 (a) The Walden plots for LiTFSA-PS and LiTFSA-SL systems with various lithium salt concentrations. The viscosity and the molar conductivity data for LiTFSA-SL system from Ref. 4 were also plotted shown as an open circle for comparison. (b) The plot of Arrhenius activation energies ($E_a(\eta^{-1})$) of viscosity vs. that for ionic conductivity ($E_a(\sigma)$) for LiTFSA mixtures of PS and SL with various lithium salt concentrations in the temperature range from 10 to 85 °C. Arrhenius equation is shown as following: $\sigma = \sigma_0 \exp(-E_a(\sigma)/RT)$, $\eta^{-1} = \eta_0^{-1} \exp(-E_a(\eta^{-1})/RT)$, where σ_0 (mS cm^{-1}) η_0 (Pa S) are the pre-exponential factor of the ionic conductivity and viscosity, respectively, R and T is ordinary meanings. (c) Left axis: self-diffusion coefficients of ^{7}Li (red), ^{19}F (blue), ^{1}H (green) obtained from the PFG-NMR for Li salts-PS systems (Li salt: PS by molar ratio) containing LiTFSA (x_{Li} = 0.333) at 298 K, where, x_{Li} is more fraction of Li salt. Right axis: Li^+ transference numbers (t_{LiNMR}) calculated based on the Nernst-Einstein relationship. The self-diffusion coefficients and t_{LiNMR} for LiTFSA-SL systems at 303 K were represented as comparison. [11]

As shown in Fig. S1a, the plots pf the PS system was located below the ideal Walden line, though those of the SL system was slightly over ideal line at the highest Li salt concentration. In Fig. S1b, values that are above the diagonal line indicate the activation energy of ionic conductivity less than that of viscosity, which is common for the ordinary dilute solutions. For both systems, the plots were above the diagonal line and shifted toward upper region with increasing Li salt concentration. The deviation from the diagonal line for the PS system was further than that for the SL system at the highest Li salt concentration, which probably due to the higher permittivity of the PS solvent i.e., more structured than the SL solutions, although the viscosity of the LiTFSA-PS solution at highest Li salt concentration was almost identical to that of the SL system. In Fig. S1c, the self-diffusion coefficient, D of the ^{7}Li for PS system was greater than that of the anion, while less than that of the solvent, similarly to the SL system, thus the transference numbers for both systems were comparable of around 0.6.

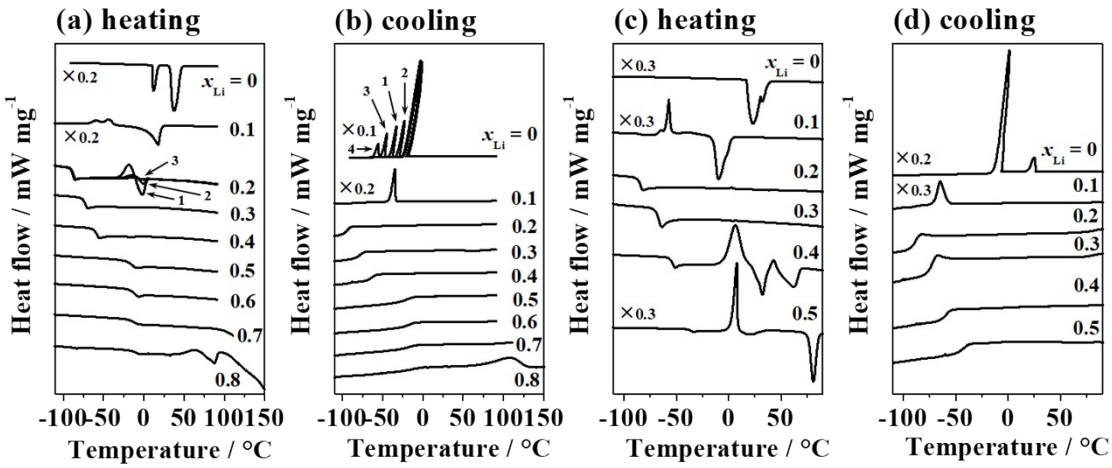

Fig. S2 Differential scanning calorimetry, DSC thermograms of (a, b) LiTFSA-PS and (c, d) LiTFSA-SL mixtures in dependence on mole fractions of Li salts x_{Li} during heating and colling cycles flowing a high purity Ar gas at 5 K min^{-1}. DCS measurements were performed for four cycles. All DSC thermograms obtained at the given composition were averaged without the first one except for LiTFSA-PS mixture (x_{Li} = 0 and 0.2).

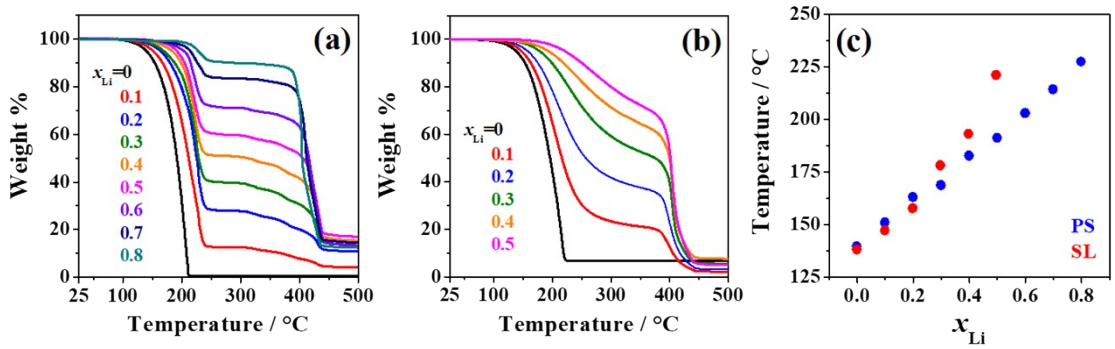

Fig. S3 Thermogravimetry TG thermograms of (a) LiTFSA-PS and (b) LiTFSA-SL mixtures in dependence on mole fractions of Li salts x_{Li} flowing a high purity Ar gas at room temperature to 500 °C. (c) temperature at which weight loss is less than 5% in dependence on mole fractions of Li salts. LiTFSA-PS and LiTFSA-SL mixtures are shown in black and red circles.

As shown in Fig. S3a and b, the temperature of the weight loss shifted to higher temperature with increasing the Li salt concentration for both systems. For PS system, the plateaus were observed over about 240 °C. As shown in Fig. S3c, the temperature for the 5 % of the weight loss was comparable for the both systems below x_{Li} = 0.3, while those for the PS system was lower than that in the SL system above x_{Li} = 0.3.

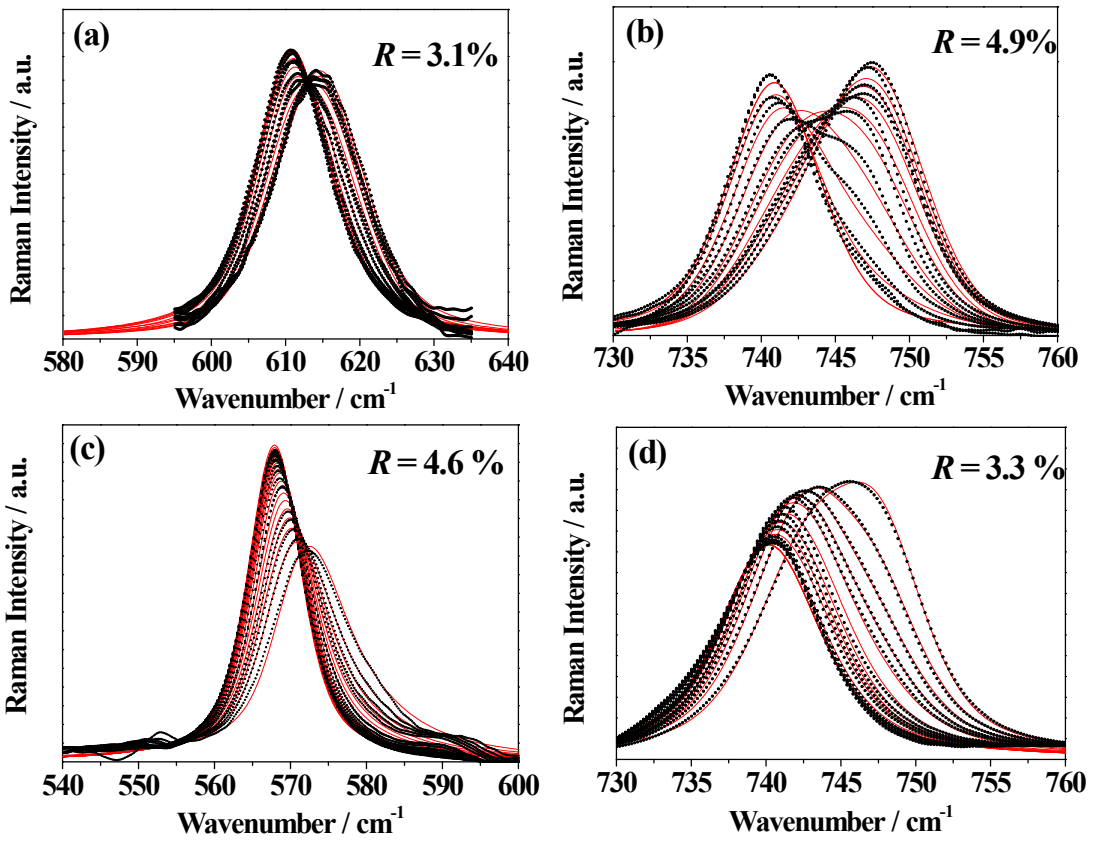

Fig. S4 Raman spectra for (a) PS, (b) TFSA in LiTFSA-PS system, (c) SL and (d) TFSA in LiTFSA-SL system with various Li salt concentrations at 298 K. Experimental and calculated Raman spectra are shown with black dots and red solid lines, respectively. Hamilton R factors ($R\ (\%) = \sqrt{\frac{\sum (I_{calc} - I_{obs})^2}{\sum I_{obs}^{\ 2}}} \times 100$) were represented in each figure. Raman bands of the LiTFSA-SL system in 540-600 cm^{-1}, which originates from the SO_2 scissoring vibration of SL, are normalized with the ring C-C stretch vibrations of the SL at 873 cm^{-1}. [12]. Similarly, the Raman band at 904 cm^{-1} used for normalization for LiTSA-PS system, which arises from PS by taking consideration of analogy, though the potential energy distribution has not reported yet. The Raman spectra in the frequency range of 730-760 cm^{-1} originates from the CF_3 bending vibration coupled with the S-N-S stretching vibration of the TFSA anion. [13, 14]

The Raman bands in 580-640 cm^{-1} for PS and 820-940 cm^{-1} for SL were overlapped with those from TFSA, so that the Raman bands from TFSA was subtracted from the observed spectra with the calculated ones based on the LiTFSA:H_2O = 1:15 solution [15] by the curve-fitting using the sum of *pseudo*-Viogt functions. Similarly, the Raman bands

from PS or SL were subtracted from the observed 730-760 cm^{-1} Raman bands from TFSA.

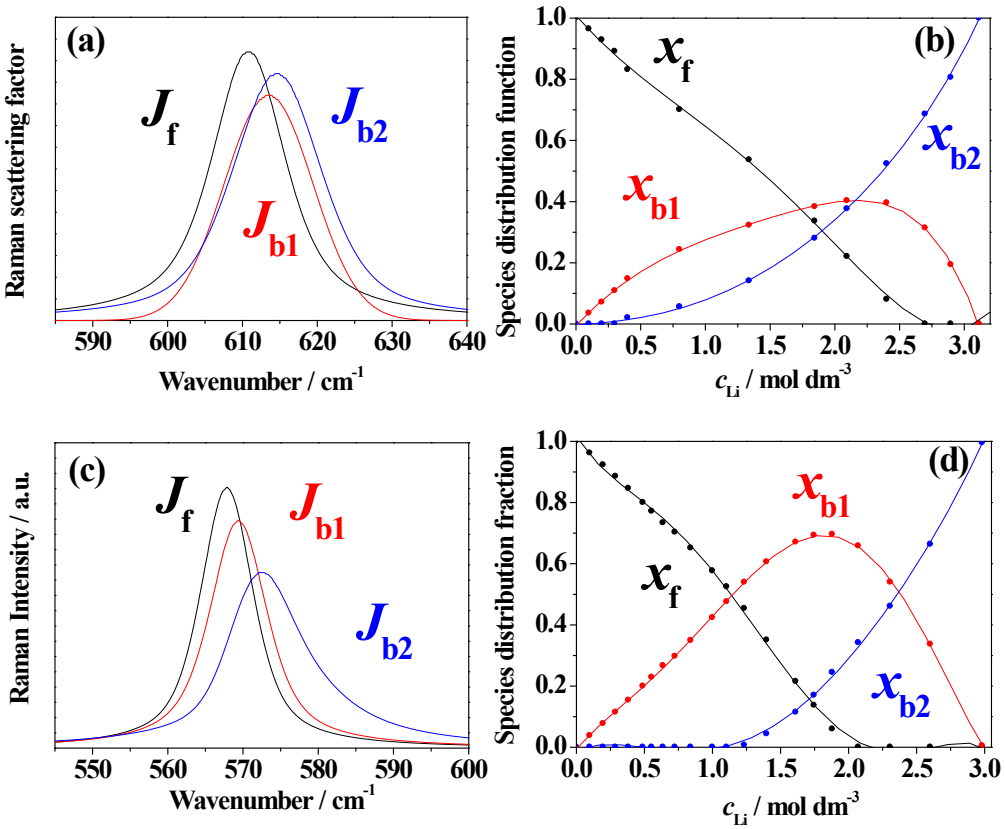

Fig. S5 The Raman scattering factors for (a) LiTFSA-PS and (c) LiTFSA-SL systems, as well as the formation distribution functions for (b) PS and (d) SL systems, were evaluated using the CLSA. Free (J_f), bound1 (J_{b1}) and bound2 (J_{b2}) of solvent are shown in black, red and blue, respectively. Mole fractions of free x_f, bound1 x_{b1} and bound2 x_{b2} is drawn in the same color of the corresponding Raman scattering factors. Details of the CLSA procedure were described in Ref. 16.

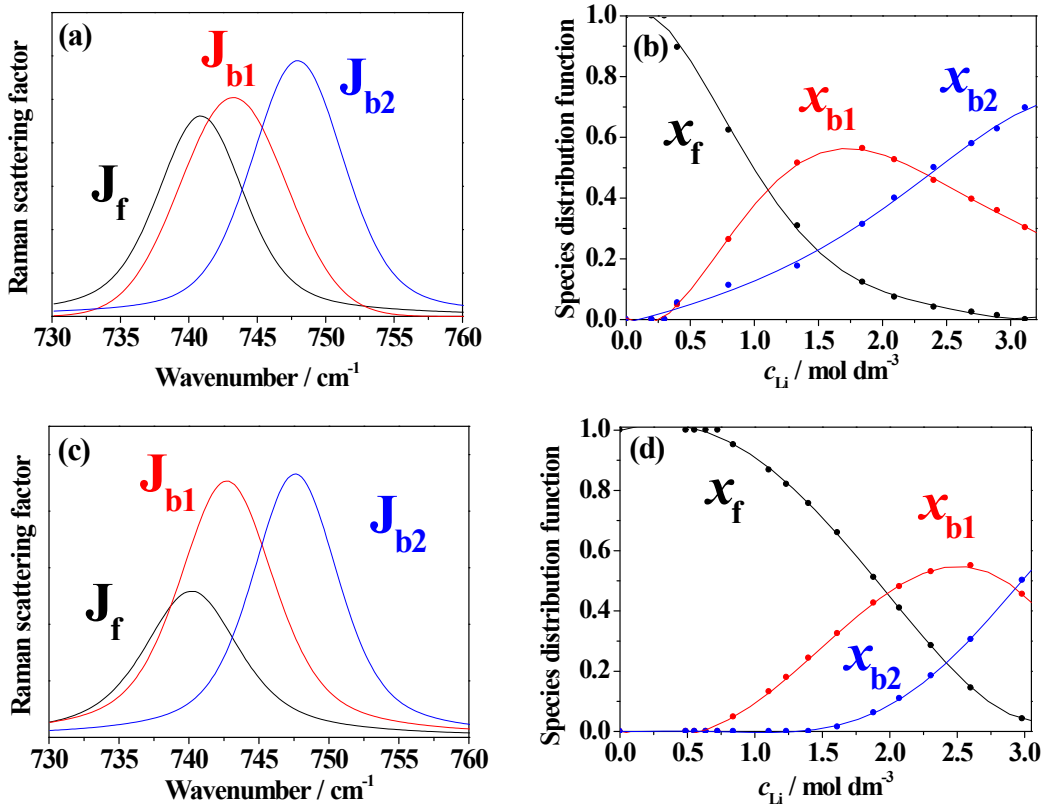

Fig. S6 The Raman scattering factors for (a) LiTFSA-PS and (c) LiTFSA-SL systems, as well as the formation distribution functions for (b) PS and (d) SL systems, were evaluated using the CLSA. Free (J_f), bound1 (J_{b1}) and bound2 (J_{b2}) of TFSA are shown in black, red and blue, respectively, for LiTFSA-PS and LiTFSA-SL systems. Mole fractions of free x_f, bound1 x_{b1} and bound2 x_{b2} is drawn in the same color of the corresponding Raman scattering factors.

The peak positions of J_f were comparable for both systems. In addition, the peak positions of J_{b1} and J_{b2} were sifted to high wavenumber side compared to that of J_f. The shift range of the peak position between these Raman scattering factors for PS system was larger than that for SL system. It suggests that the PS have a weaker interaction with Li^+ compared to SL so that the CIP/AGG is more likely to form in the LiTFSA-PS solutions.

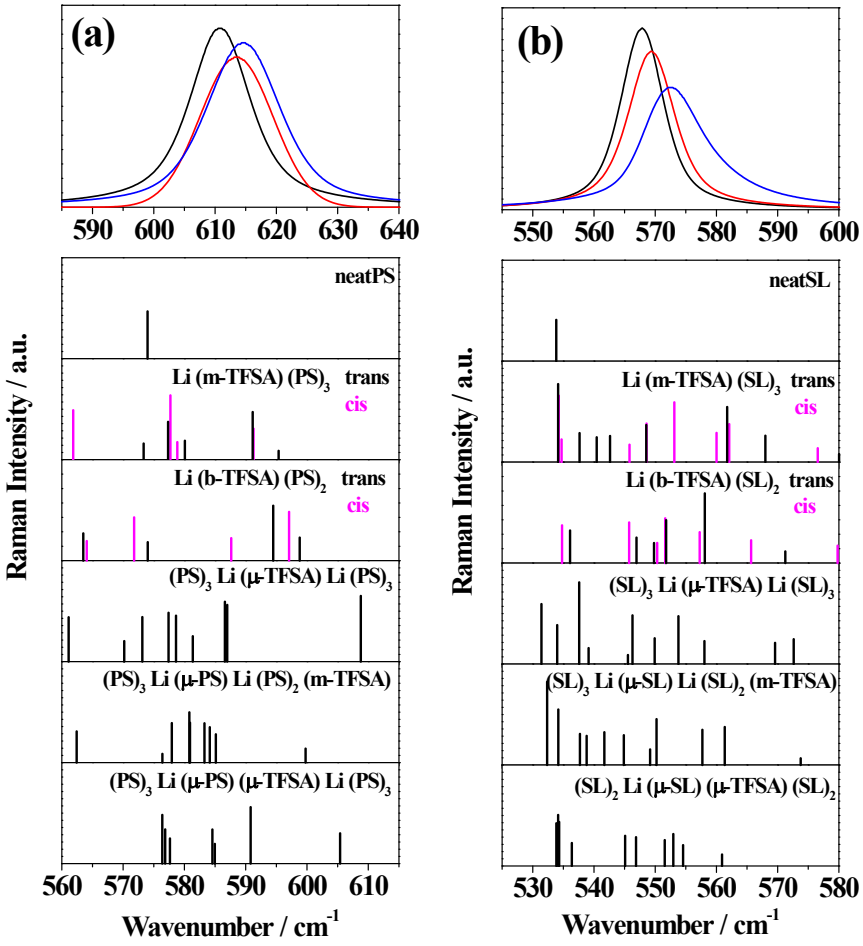

Fig. S7 Raman scattering factor (Top), J_f (black), J_{b1}(red), J_{b2} (blue) of solvents for (a) LiTFSA-PS and (b) LiTFSA-SL from CLSA. Theoretical Raman bands (bottom) for the corresponding optimized geometries of isolated solvent and Li ion complexes. m, b and μ are the monodentate ligand, the bidentate ligand and the bridging ligand. The optimized structure described in Fig. S9 and S10.

As for PS system, J_f. is in acoordance with the theoritical Raman band frequency of 574 cm^{-1} for the isolated PS in the gas phase. On the other hands, J_{b1} and J_{b2} could be explained with several theoritical Raman bands; J_{b1} can be attributed to the monomeric CIP models like Li(m-TFSA)PS_3 and Li(b-TFSA)PS_2 additional to the fully solvated Li^+ of $[Li(PS)_4]^+$, similarly J_{b2} can be ascribable to the CIP/AGG models such as $(PS)_3$Li(μ-TFSA)Li$(PS)_3$, $(PS)_2$TFSALi(μ-PS)Li $(PS)_3$, $(PS)_2$Li(μ-PS)(μ-TFSA)Li$(PS)_3$. The similar discussion can be applied to the the SL system.

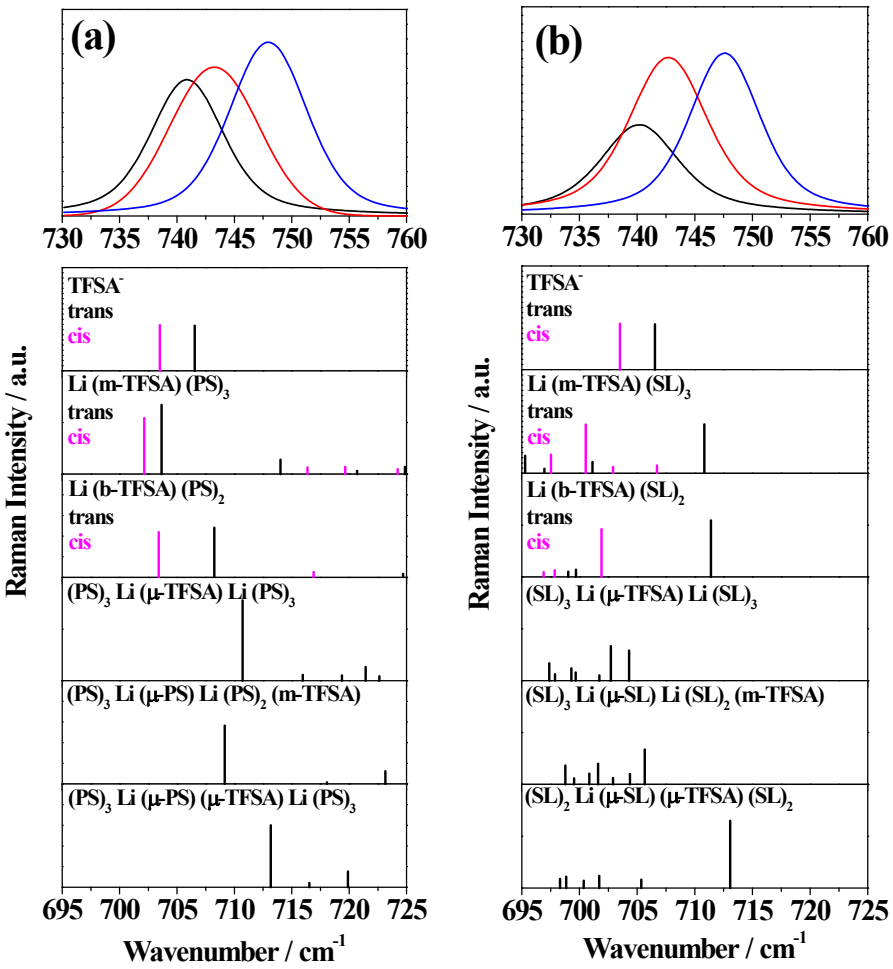

Fig. S8 Raman scattering factor (Top), J_f (black), J_{b1}(red), J_{b2} (blue) of TFSA anion for (a) LiTFSA-PS and (b) LiTFSA-SL from CLSA. Theoretical Raman bands (bottom) for the corresponding optimized geometries of isolated solvent (S; PS or SL), TFSA anion and Li ion complexes, where m, b and μ are the monodentate ligand, the bidentate ligand and the bridging ligand. The optimized structure described in Fig. S9 and S10.

[Li(b-TSFA)$(PS)_2$] containing *trans* TFSA can explicate J_{b1} because its theoritical Raman band shifts to the higher frequency relative to the isolated TFSA in the gas phase. Similarly, J_{b2} can be explained with the AGG models including bridged TFSA such as [$(PS)_3$Li(μ-TFSA)Li$(PS)_3$] abnd [$(PS)_3$Li(μ-PS)(μ-TFSA)Li$(PS)_3$]. On the other hand, with regard to the SL system, J_{b1} and J_{b2} could be explained with both of [Li(m-TSFA)(SL_3) and [Li(b-TSFA)$(SL)_2$]] ciontaining trans TFSA as a CIP model and [$(SL)_3$Li(μ-PS)(μ-TFSA)Li$(SL)_3$] as a AGG model, respectively. [$(SL)_3$Li(μ-TFSA) Li$(SL)_3$] and [$(SL)_3$Li(μ-TFSA) Li$(SL)_2$(m-TSFA)] could contribute to the J_{b1}.

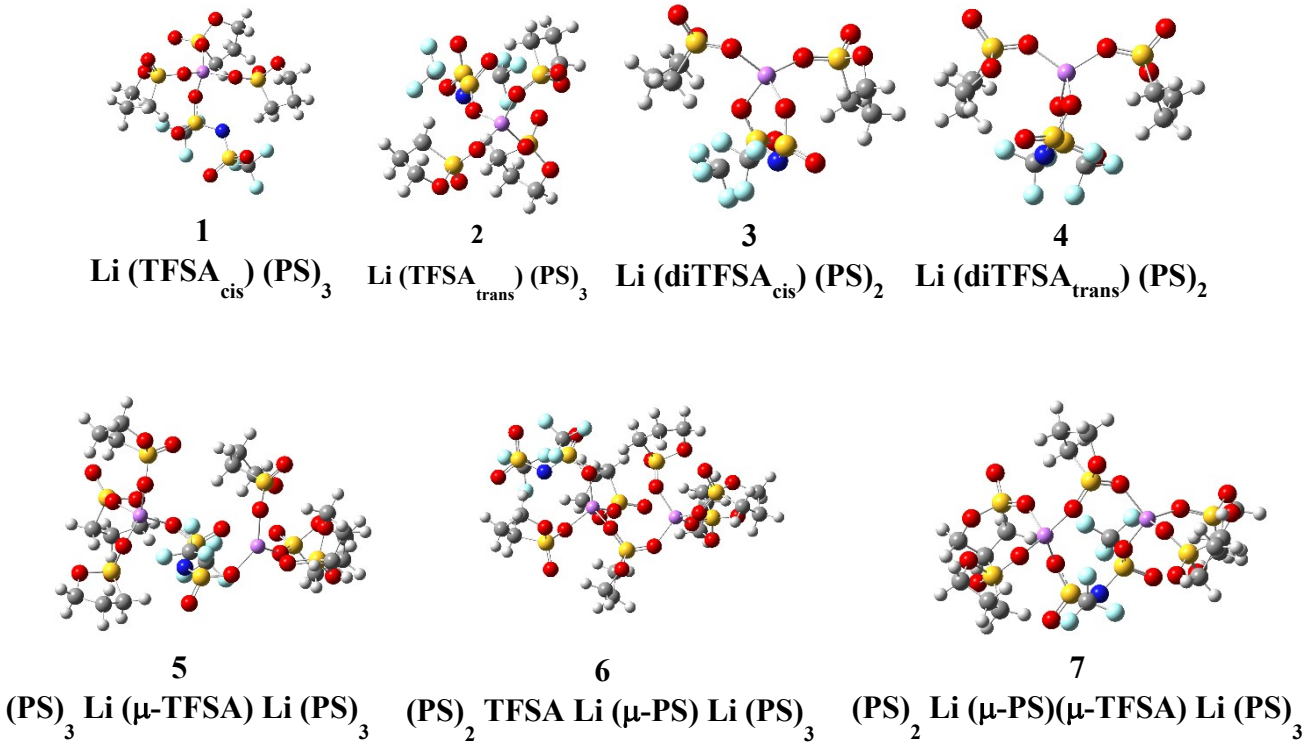

Fig. S9 The optimized geometries of Li ion complexes calculated at the B3LYP/cc-pVDZ level by using Gaussian 16.

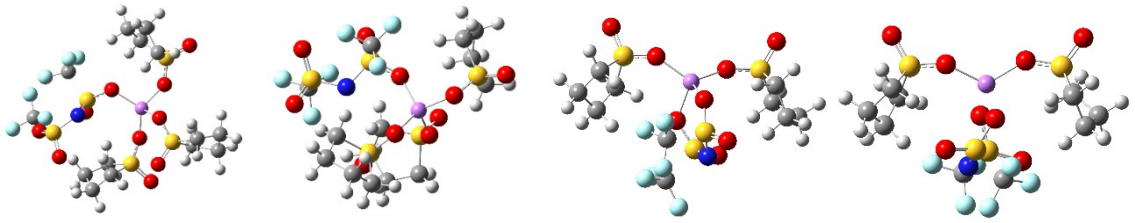

1 **2** **3** **4**

Li (TFSA$_{cis}$) (SL)$_3$ **Li (TFSA$_{trans}$) (SL)$_3$** **Li (diTFSA$_{cis}$) (SL)$_2$** **Li (diTFSA$_{trans}$) (SL)$_2$**

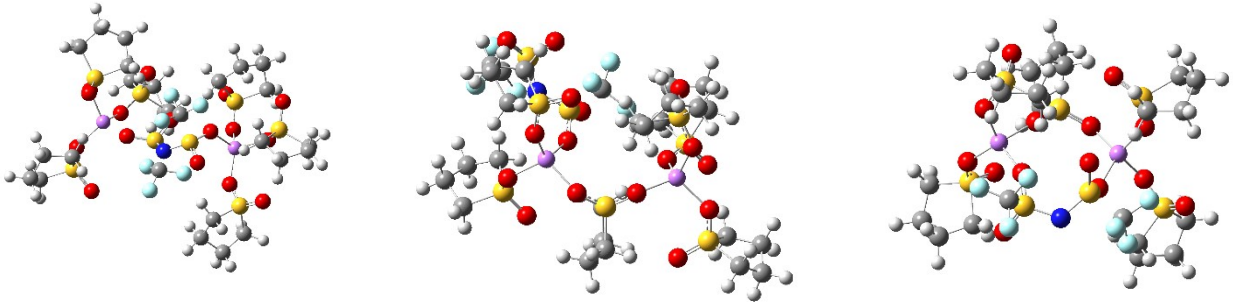

5 **6** **7**

(SL)$_3$ Li (μ-TFSA) Li (SL)$_3$ **(SL)$_2$ TFSA Li (μ-SL) Li (SL)$_3$** **(SL)$_2$ Li (μ-SL)(μ-TFSA) Li (SL)$_3$**

Fig. S10 The optimized geometries of Li ion complexes calculated at the B3LYP/cc-pVDZ level by using Gaussian 16.

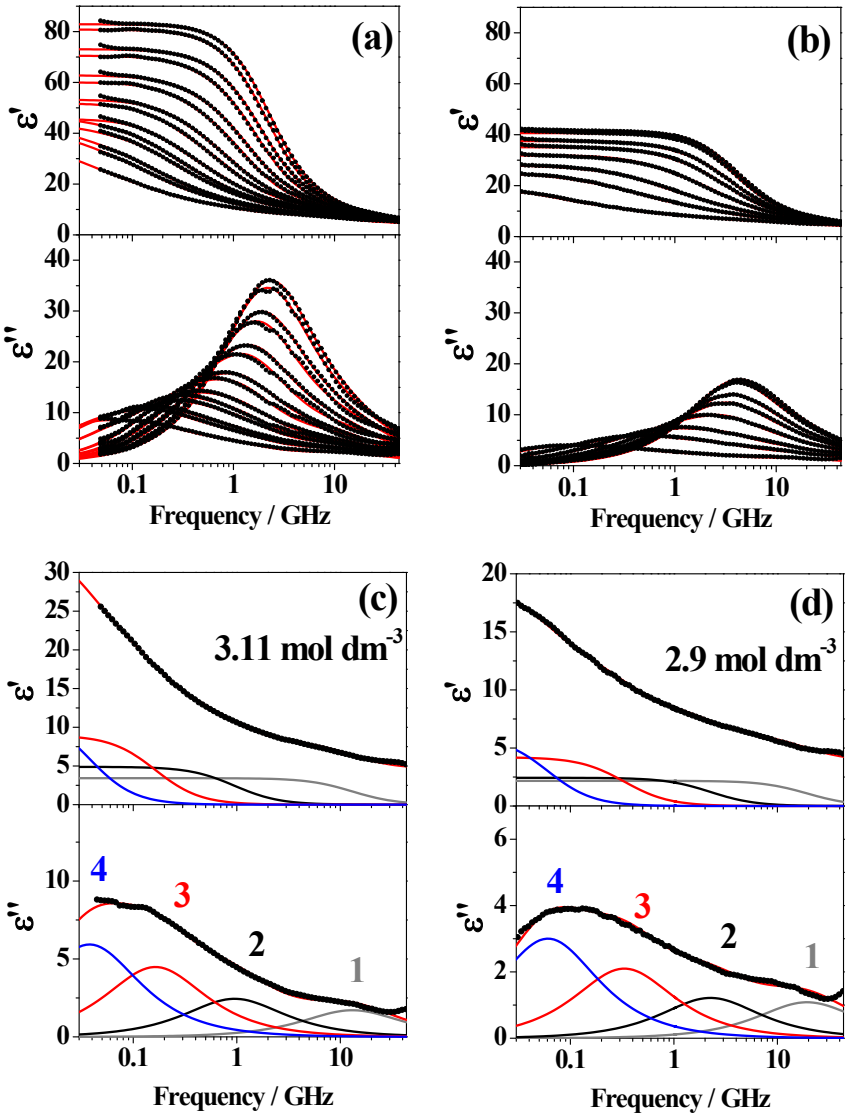

Fig. S11 Dielectric relaxation spectra for (a) LiTFSA-PS (c_{Li} = 0.10 – 3.11 mol dm^{-3}) and (b) LiTFSA-SL (c_{Li} = 0.099 – 2.9 mol dm^{-3}) systems. Typical fitting results for (c) LiTFSA-PS (c_{Li} = 2.9 mol dm^{-3}) and (d) LiTFSA-SL (c_{Li} = 3.11 mol dm^{-3}) systems. The observed and calculated data are indicated in black dots and red solid lines. The calculated dielectric relaxation was expressed as the superposition of the Debye relaxation model; $\hat{\varepsilon}(\nu) = \varepsilon_\infty + \sum_i \frac{S_i}{1 + \mathrm{i}2\pi\nu\tau_i}$ where ε_∞, ν, S_i and τ_i stand for the relative permittivity at the infinite frequency, frequency, a relaxation strength and a relaxation time for the *i*th dipole, respectively. The component relaxations are shown in gray, black, red and blue lines for i = 1, 2, 3 and 4, respectively. The mode 1 could come from the inter-molecular vibration and hence will not be discussed further.

The static permittivity of the PS system was noticeably higher than that of SL system. The re-orientational relaxation of the PS and SL solvent dipole was observed at the frequency of around 2 GHz and 5 GHz, respectively. For both systems, the intensity of this relaxation decreased and shifted to the lower frequency side by adding the lithium salt. A new relaxation at around 1 GHz was appeared with increasing the lithium salt concentration, followed by the intensity decrease and shift to 0.4 GHz. At the highest lithium salt concentration, the slowest relaxation was observed below and around 50 MHz for PS and SL system, respectively.

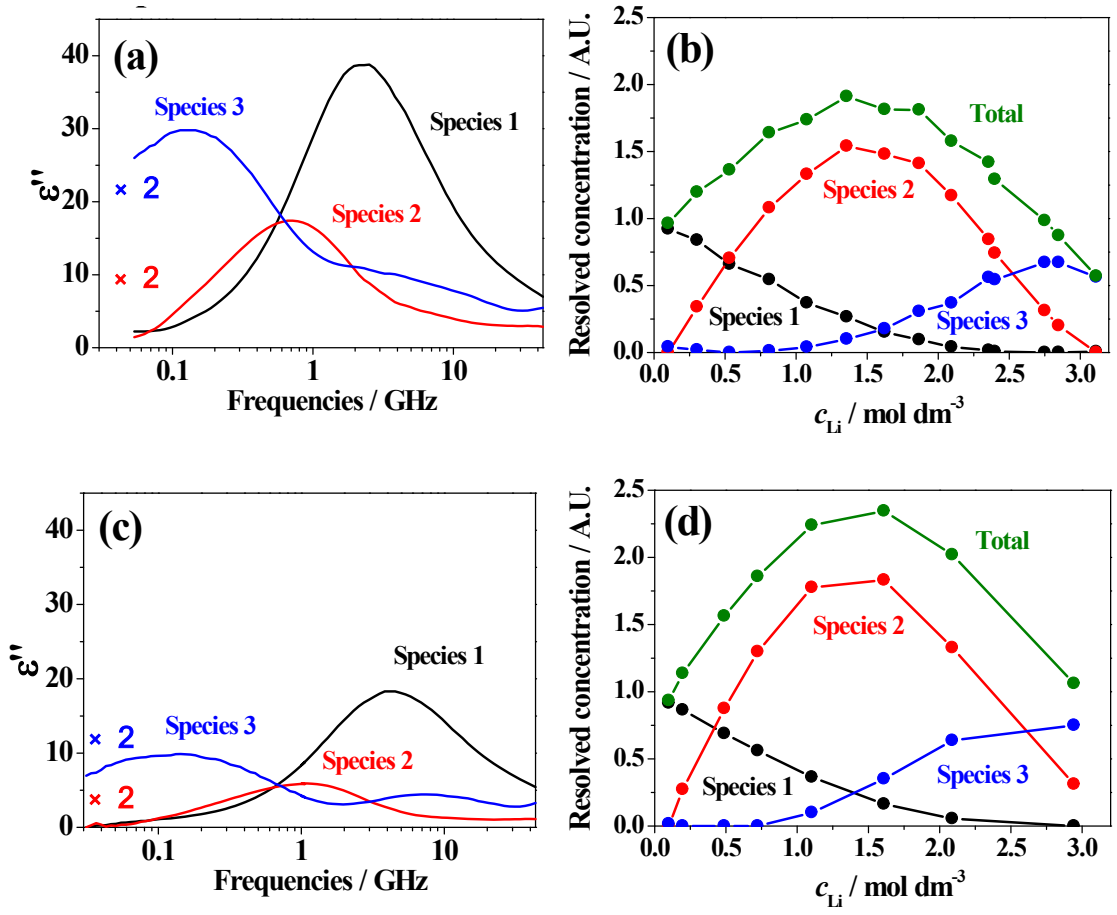

Fig. S12 Left panels: the resolved spectra evaluated with the MCR-ALS for (a) PS and (c) SL systems. Right panels: the resolved concentrations evaluated with the MCR-ALS for (b) PS and (d) SL systems. Details of the MCR-ALS procedure were described in Ref.17 and 18. The intensity of the relaxations for the species 2 and 3 was doubled for comparison to that for the species 1.

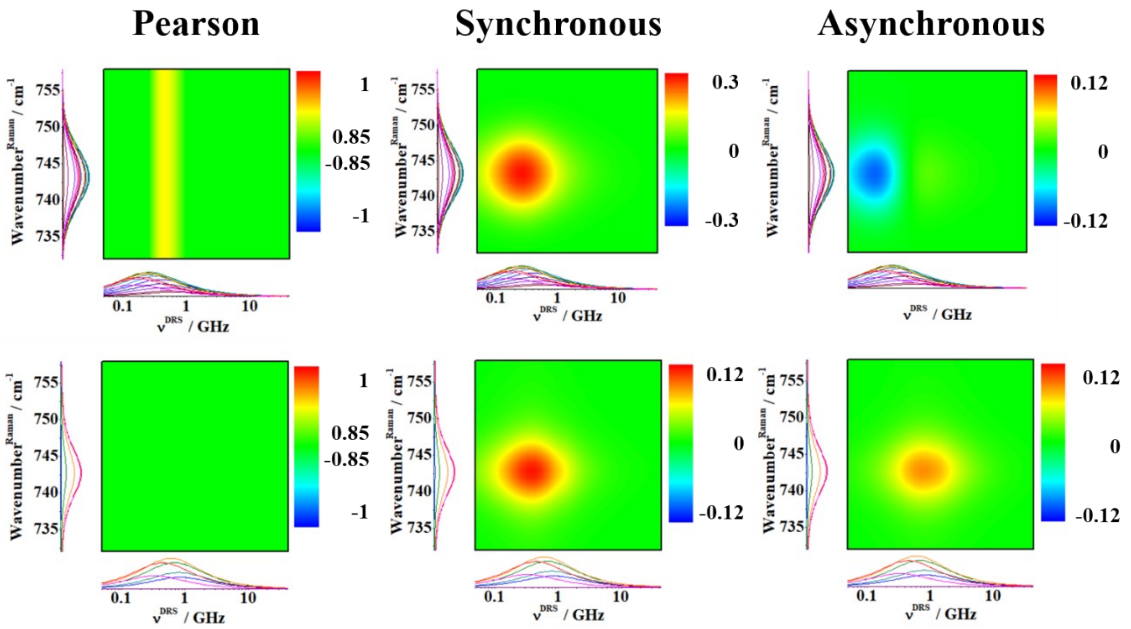

Fig. S13 2D correlation analysis between the calculated Raman spectra of TFSA anion and the calculated dielectric loss (imaginary part of the complex permittivity). Left panels show the Pearson correlation coefficients, middle and right display synchronous and asynchronous correlation of the Noda-Ozaki 2D hetero-correlation spectroscopy, respectively. Noda-Ozaki 2D correlation spectroscopy is normalized with the maximum absolute value among the synchronous correlation. Red and blue represent high positive and negative correlation, respectively. Green corresponds to results within a value of 0.85 in the Pearson correlation coefficients and around 0 in the Noda-Ozaki 2D hetero-correlation spectroscopy. The color mapping for asynchronous correlation is expanded by a factor of 2.5 due to the weak correlation. The upper and lower panels are results for LiTFSA-PS and LiTFSA-SL systems, respectively. The Raman spectra were obtained by using the Raman scattering factors (J_{b1}) and concentration (x_{b1}) of anion bound 1 species. The dielectric loss spectra were obtained by using the $i = 3$ Debye relaxation mode.

For the PS system, the Pearson's correlation coefficients and the Noda-Ozaki synchronous correlation exhibited correlation to some extent between the intermediated relaxation with the Raman spectra obtained by anion bound 1 species. As clearly indicated in the Noda-Ozaki synchronous and asynchronous correlations, there were positive and negative correlations at around 0.2 GHz and 0.1 GHz, respectively. On the other hands, as for the SL systems, no clear correlation was found in the Pearson's correlation coefficients. The both synchronous, and asynchronous of the Noda-Ozaki 2D hetero-

correlation spectroscopy exhibited positive correlations at around 0.2 and 1 GHz, respectively.

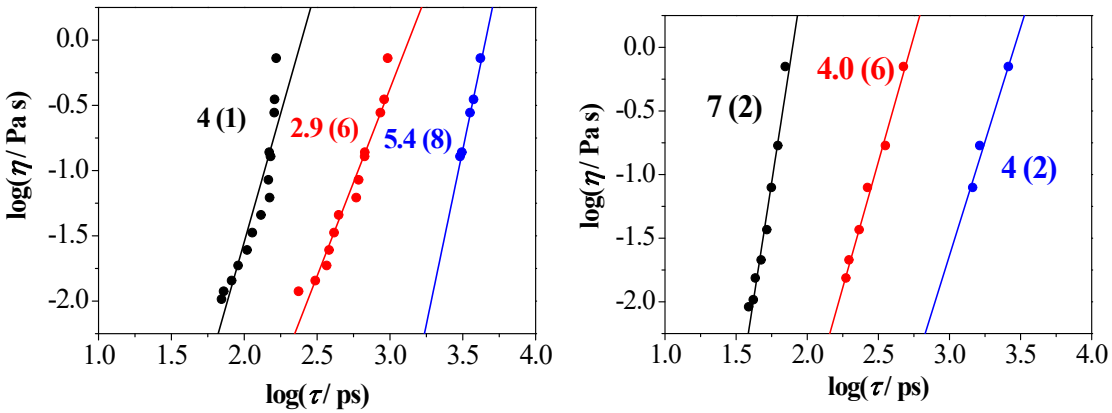

Fig. S14 Relationship between viscosity and τ_i for (a) LiTFSA-PS and (b) LiTFSA-SL systems are represented in left and right panels, respectively. The numbers and those in parenthesis are the respective slope and the corresponding standard deviations.

References

1. Y.-C. Chiu and R. M. Fuoss, *J. Phys. Chem.* 1968, **72**, 12, 4123–4129.
2. E. O. Stejskal, *J. Chem. Phys.* 1965, **43**, 3597–3603.
3. M. J. Frisch, G. W. Trucks, H. B. Schlegel, G. E. Scuseria, M. A. Robb, J. R. Cheeseman, G. Scalmani, V. Barone, G. A. Petersson, H. Nakatsuji, X. Li, M. Caricato, A. V. Marenich, J. Bloino, B. G. Janesko, R. Gomperts, B. Mennucci, H. P. Hratchian, J. V. Ortiz, A. F. Izmaylov, J. L. Sonnenberg, D. Williams-Young, F. Ding, F. Lipparini, F. Egidi, J. Goings, B. Peng, A. Petrone, T. Henderson, D. Ranasinghe, V. G. Zakrzewski, J. Gao, N. Rega, G. Zheng, W. Liang, M. Hada, M. Ehara, K. Toyota, R. Fukuda, J. Hasegawa, M. Ishida, T. Nakajima, Y. Honda, O. Kitao, H. Nakai, T. Vreven, K. Throssell, J. A. Montgomery, Jr., J. E. Peralta, F. Ogliaro, M. J. Bearpark, J. J. Heyd, E. N. Brothers, K. N. Kudin, V. N. Staroverov, T. A. Keith, R. Kobayashi, J. Normand, K. Raghavachari, A. P. Rendell, J. C. Burant, S. S. Iyengar, J. Tomasi, M. Cossi, J. M. Millam, M. Klene, C. Adamo, R. Cammi, J. W. Ochterski, R. L. Martin, K. Morokuma, O. Farkas, J. B. Foresman and D. J. Fox, *Gaussian 16, Revision C.01, Gaussian, Inc.*, *Wallingford CT*, 2016.
4. T. Sonnleitner, D. A. Turton, S. Waselikowski, J. Hunger, A. Stoppa, M. Walther, K. Wynne, R. Buchner, *J. Mol. Liq.* **2014**, 192, 19– 25.
5. U. Kaatze and V. Uhlendorf, *Z. Physik. Chem.* **1981**, 126, 151-165.
6. J. Barthel, K. Bachhuber, R. Buchner, J. B. Gill, M. Kleebauer, *Chem. Phys. Lett.* **1990**, 167, 62.
7. J. Barthel, J., R. Buchner, B. Wurm, *J. Mol. Liq.* **2002**, 98-99, 51–69.
8. I. Noda and Y. Ozaki, *John Wiley & Sons*, 2005.
9. I. Noda, *Applied Spectroscopy* 2000, **54**, 994-999.
10. https://sites.google.com/view/shigemorita/home/2dshige
11. A. Nakanishi, K. Ueno, D. Watanabe, Y. Ugata, Y. Matsumae, J. L. Liu, M. L. Thomas, K. Dokko and M. Watanabe, *Journal of Physical Chemistry C*, 2019, **123**, 14229-14238.
12. J. E. Katon and W. R. Feairheller, *Spectrochimica Acta* 1965, **21(1)**, 199–201.
13. I. Rey, P. Johansson, J. Lindgren, J. C. Lasse`gues and J. Grondin, *J. Phys. Chem. A* 1998, **102**,3249.
14. Y. Umebayashi, S. Mori, K. Fujii, S. Tsuzuki, S. Seki, K. Hayamizu and S. Ishiguro, *J. Phys. Chem. B* 2010, **114**, 6513–6521.
15. H. Watanabe, N. Arai, E. Nozaki, J. Han, K. Fujii, K. Ikeda, T. Otomo, K. Ueno, K. Dokko, M. Watanabe, Y. Kameda, and Y. Umebayashi, *J. Phys. Chem. B* **2021**, 125, 27, 7477–7484.

16. N. Arai, H. Watanabe, E. Nozaki, S. Seki, S. Tsuzuki, K. Ueno, K. Dokko, M. Watanabe, Y. Kameda and Y. Umebayashi, *J. Phys. Chem. Lett.* 2020, **11**, 11, 4517–4523.
17. M. Esteban, C. Ariño, J. M. Dı́az-Cruz, M. S. Dı́az-Cruz and R. Tauler, *Trends Anal. Chem.* **2000**, 19, 49-61.
18. J. Jaumot, R. Gargallo, A. de Juan and R. Tauler, *Intell. Lab. Syst.* **2005**, 76, 101–110.